



HAL
open science

High power laser heating of nuclear ceramics for the generation of controlled spatiotemporal gradients

Matthieu Reymond, Thomas Doualle, Jerome Sercombe, Mathilde Rocca, Mehdi Nasselahsen, Christian Colin, Yves Pontillon, Laurent Gallais

► **To cite this version:**

Matthieu Reymond, Thomas Doualle, Jerome Sercombe, Mathilde Rocca, Mehdi Nasselahsen, et al.. High power laser heating of nuclear ceramics for the generation of controlled spatiotemporal gradients. Journal of Applied Physics, 2023, 134 (3), pp.033101. 10.1063/5.0146541 . hal-04412911

HAL Id: hal-04412911

<https://hal.science/hal-04412911v1>

Submitted on 14 Feb 2024

HAL is a multi-disciplinary open access archive for the deposit and dissemination of scientific research documents, whether they are published or not. The documents may come from teaching and research institutions in France or abroad, or from public or private research centers.

L'archive ouverte pluridisciplinaire **HAL**, est destinée au dépôt et à la diffusion de documents scientifiques de niveau recherche, publiés ou non, émanant des établissements d'enseignement et de recherche français ou étrangers, des laboratoires publics ou privés.

High power laser heating of nuclear ceramics for the generation of controlled spatio-temporal gradients

Matthieu Reymond^{a,b}, Thomas Doualle^a, Jerome Sercombe^a, Mathilde Rocca^a, Mehdi Nasselahsen^a, Christian Colin^a, Yves Pontillon^a and Laurent Gallais^b.

a, CEA, DES, IRESNE, DEC, Cadarache F-13108 Saint-Paul-Lez-Durance, France

b, Aix Marseille Univ, CNRS, Centrale Marseille, Institut Fresnel, Marseille, France

Abstract:

The use of high-power laser to reach the high-temperatures typical for off-normal conditions in nuclear reactor fuel or to determine its properties at high temperature is a relevant and proven technique in the nuclear research community. Conducting studies at high temperature with full control in space and time of the thermal gradients is however a challenge. In this paper, we present a combination of methodologies, experiments and models to drive nuclear fuel samples in thermal conditions relevant to the study of nuclear fuel materials. Based on the use of high-power (kW) lasers with beam shaping and temporal laser control, our experimental approach allows one to heat depleted UO_2 samples and obtain precise control of the temporal gradients, in the ms range, and spatial gradients, in the 100 μm range. The coupling with numerical simulations allows one to determine the temperature distribution in the depth of the sample and to develop a thermo-mechanical interpretation of the results. We will present the methodology allowing one to properly compare experimental and simulation results by taking into account the optical response of the instrumentation, the laser- UO_2 interaction and the resulting heat source term. We will show that we can express the heat source term resulting from the laser loading either by an analytical description or statistically based on Monte-Carlo simulation. A fairly good agreement between the recorded temperature and the simulation results is shown. The presented methodology can be extended to other materials with a proper choice of laser wavelength and instrumentation based on the optical properties of the investigated material.

1. Introduction:

Laser heating is a routinely used technique in various fields to weld, cut, vaporize or anneal materials. It is also used to study materials at high temperature [1–4]. In the nuclear research community, laser heating is used to study nuclear materials properties at high temperature or to investigate its behavior under off-normal conditions. We can cite for example the work carried out at the Institute for Transuranium Elements (Karlsruhe, Germany) for the determination of the fusion point of various nuclear materials [5–8] or the determination of thermo-physical properties such as the thermal diffusivity, thermal conductivity or specific heat of UO_2 [9–11]. Other notables studies include the study of the optical properties of solid and liquid UO_2 heated by laser by Bober et al [12,13] or spectrometric analysis of laser induced vapors of UO_2 by M. Joseph et al [14] and R. Pfiogler et al [15].

The work presented hereinafter is part of recent developments, conducted in the framework of nuclear fuel research at CEA (French Atomic Energy Commission), based on a multi-objective laser platform for the study of nuclear fuel in accidental conditions [16,17] or the determination of thermo-physical properties at high-temperatures [18].

These studies are enabled by the fact that laser heating is allowing one to heat any absorbing material of interest to extreme temperature with an unmatched precision regarding the spatial or temporal energy deposition in the sample. The temperature rising rate can also be finely tuned, depending on the pulse duration, the available laser power, absorption of the considered material and heated surface. The laser-heating approach can also be easily coupled with contactless instruments such as pyrometers, infrared cameras, spectrometers, optical microscopy, or any other relevant instrumentation.

However, this approach often needs to be coupled with the precise simulation of the heating sequence if one wishes to interpret experimental results in a meaningful way. In particular, the non-isothermal conditions induced by laser-heating often makes the interpretation of the results difficult without the modeling of the experiment. Above all, the internal temperature gradient in the depth of the sample cannot be observed nor measured. The simulation of the experiment is thus essential to properly interpret the results. This remark is particularly true under non-steady state condition. Finally, the deduction of the mechanical load induced by the thermal gradient also necessitates a thermal and mechanical numerical model.

In this paper, we present laser-heating experiments of various duration (ms range), power, and intensity distributions of the used laser pulse(s) conducted on depleted polycrystalline UO_2 disks aiming to induce fast heating ($>10\,000\text{ K/s}$) with a precise control of the spatial gradient in order to reach thermal conditions representative of accidental conditions encountered in a nuclear plant such as the Reactivity Initiated Accident (RIA) [16,19]. The temperature evolution during these parametric studies are obtained through thermographic imaging means and compared to simulations performed with a numerical model based on the finite element method using the thermal solver Cast3m [20] developed by the CEA.

In order to thoroughly analyze the results through numerical means, we first performed the optical characterization of the considered nuclear ceramic. Indeed, the knowledge of the optical properties of the material is important to accurately describe the absorption of the laser radiation by the samples. To do so, we realized reflectance and transmittance measurements from which we deduced the complex refractive index of the ceramic. Then, experimental techniques and methods used to realize the laser heating experiments are presented. In a second time, we present the numerical model used, the associated material parameters and the description of the heat load resulting from the laser beam propagation and absorption in the depth of the sample. We propose two methods to describe the laser induced heat source term, either by an analytical description or statistically by a preliminary step of Monte-Carlo simulation for light propagation in the sample. The later allowed the phenomenological study of the potential contribution in the simulations and resulting temperature fields of the scattering phenomenon. A fairly good agreement between the recorded temperature and the simulation results was obtained, indicating that all the relevant phenomena are taken into account.

To conclude, laser beams of different intensity profiles were combined in order to reach RIA like thermal conditions, thus demonstrating the flexibility of the laser heating technique in terms of reachable temperature transients.

II. Experimental methods:

This work focuses on depleted UO_2 disks of thickness 0.5 or 1 mm. These disks are obtained from dense (~96-98% of the theoretical density, measured by hydrostatic weighting in alcohol) and polycrystalline UO_2 fuel pellets fabricated at CEA using a wet process followed by isostatic compaction at 450 MPa and sintering at 1650 °C during 2h under flowing H_2 . These pellets have a diameter of around 8.2 mm and a height of around 13.5 mm. They were manufactured without dishes or chamfers, as opposed to their industrial versions. Their average grain size is about 10 μm . The disks were obtained from the mother pellets with a wire saw and consequently, their faces presented a typical rough-cut surface rugosity.

1) Complex refractive index of polycrystalline UO_2 :

In order to describe as precisely as possible the laser loading in the simulations, a complete and thorough characterization of the optical properties of the considered material is necessary. In particular, the knowledge of the absorption and of the coefficient of absorption of the material at our laser wavelength (1080 nm) is crucial, the former describing the amount of power coupled in the material and the latter describing the depth of penetration of the incoming laser light in the material. Hence, the value of the absorption and of the coefficient of absorption intervenes at first order on the calculated temperatures at the surface and in the volume of the sample. It is thus important to determine these values.

Very few characterizations of the optical properties of UO_2 have been reported in the literature. Moreover, there are some discrepancies in the published values of optical properties of UO_2 , possibly related to differences in material composition or microstructure. We also note that almost all studies were interested in monocrystalline or amorphous UO_2 without consideration for the polycrystalline material [21–24].

Different approaches exist for the determination of the optical properties of a material, based either on spectro-photometric or ellipsometric measurements. Most studies conducted on UO_2 were based on spectro-photometric measurements such as the absorption, transmission or reflection spectra. Briefly, this approach is based on the measurements of one or more spectra (transmission, reflection or absorption) at different angles of incidence or polarization state. By direct inversion of the spectra or through numerical optimization means, one can infer the optical properties of the sample. The spectro-photometric approach is also suitable for scattering samples and is thus more general.

Consequently, the complex refractive index of UO_2 was determined in the visible and near-infrared wavelength range (500 – 1100 nm) from spectrophotometric reflectance and transmittance measurements performed on thin samples of thicknesses inferior to 55 μm . Two methods were used to deduce the complex refractive index from the measurements. The first one is a straightforward inverse method using analytical equations describing the light- UO_2 interaction and light propagation in the thickness of the sample while the second one is based on a more classical approach using a matrix formalism to describe light propagation in the considered optical system, combined with an appropriate dispersion model coupled with a numerical minimization algorithm. These two methods yielded similar results.

We report for the imaginary part of the refractive index k values around 0.006 below the band-gap energy, in the 650-1100 nm wavelength range. We report decreasing values of n between 2.3 to 2.0 with increasing wavelength. These values are consistent with reported values of the real part of the refractive index in the literature [12,22]. The absorption coefficient decreases from 200 000 m^{-1} at 550 nm towards a value of roughly 70 000 m^{-1} in the near-infrared part of the spectrum. Its inverse (the so-called depth of penetration) is thus around 15 μm at our laser wavelength (1080 nm).

The samples preparation, measurements, methodology and interpretation of these findings are available in this supplementary file of this study.

2) Experimental configurations:

The experiments were conducted on the CHAUCOLASE platform (CHAUFFage COntrollé par LASEr/laser-controlled heating) located at the Institut Fresnel. This platform notably consists in two continuous wave high-power Ytterbium fiber laser and a dedicated vacuum chamber equipped with multiple viewports allowing for the transmission of the laser beams and optical instrumentation. More details on this platform can be found in [25]. To avoid the oxidation of the sample during heating, the experiments were conducted under vacuum (10^{-2} mbar). From the aforementioned value of the coefficient of absorption of polycrystalline dense UO_2 , the use of Ytterbium fiber laser (wavelength 1080 nm) is pertinent to submit uranium dioxide to laser heating. The first laser used can deliver up to 1500 W of maximum power (SPI laser Qube 1500) with a mono-mode Gaussian beam and a rising time of a few microseconds. The beam is non-polarized and is characterized by a central wavelength of 1080 nm with a bandwidth <4 nm. In this study, a beam diameter of 8 mm (Gaussian distribution with a diameter defined at $1/e^2$) was used. This laser was used to generate an annular Gaussian beam with a Diffractive Optical Element (DOE, Silos Technologies) as previously described in [16,17]. This annular Gaussian beam is characterized by its radius R_{an} and waist (at $1/e^2$) ω_{an} . Two dimensions of annular beams were used in this study:

- 3.9 mm radius and 0.1 mm waist, hereinafter called focused annular beam.
- 3.660 mm radius and 0.260 mm waist, hereinafter called unfocused annular beam.

Images of these two beams profiles in the sample's plane can be viewed Figure 1.

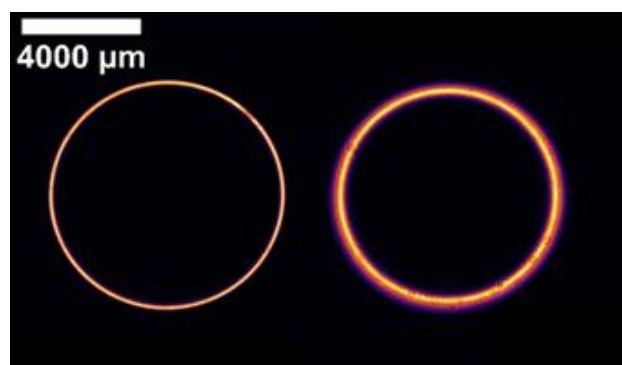


Figure 1: Left: image of the beam profile of the focused annular beam. Right: image of the beam profile of the unfocused annular beam.

A second laser was used, which can deliver up to 2000 W of maximum power with a multi-mode laser beam (SPI Laser Qube 2000). This beam was used to generate a quasi Top-Hat (TH) beam. To do so the beam is first focused with a lens of focal length 500 mm (Eksma optics, AR coated at 1064 nm), thus obtaining a beam with a diameter (at $1/e^2$) inferior to 1 mm in the focal plane. This focused beam presents an intensity profile that can be assimilated as a Top-Hat distribution (super Gaussian distribution of power 6). We then reimaged on the sample this quasi TH beam with an air-spaced achromatic doublet (Thorlabs ACA254-100-B) placed in the focal plane of the first lens. This apparatus was placed in such a way that the TH beam has a diameter slightly superior to the heated disk diameter in the image plane where the sample was placed. The obtained diameter was about 9 mm in the sample plane versus 8.2 mm for the sample diameter. An image of the beam profile and normalized profiles plot is shown Figure 2. The standard deviation measured on the normalized profile is 5%.

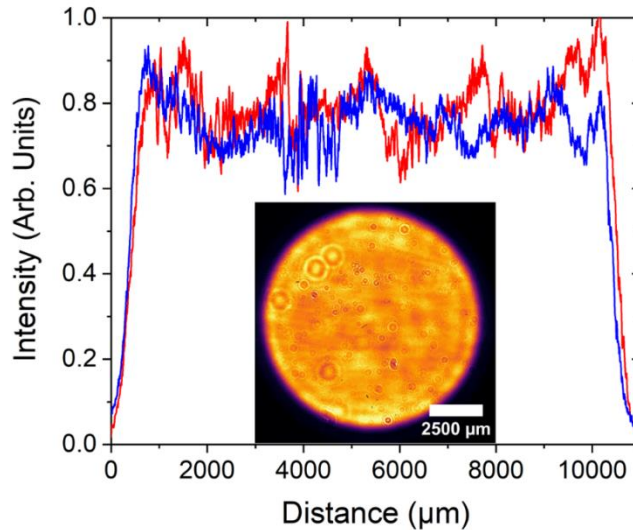


Figure 2: Horizontal and vertical normalized intensity profiles. Insert: False color image of the normalized homogeneous beam in the sample's plane.

These two beams can then be combined and adjusted in terms of dimensions, temporal profiles or power to tune the generated transient.

In this study, we used a custom sample holder (Sceram Advanced Ceramics) made of ZrO_2 with some parts made of stainless steel. This sample holder was specifically designed to ensure known thermal boundary conditions at the surfaces of the sample. It relies on the use of two jaws maintaining the sample vertically by its edge. The top jaw applies a pressure through a spring-piston system. The jaws are made of ZrO_2 , which has a low thermal conductivity, thus ensuring that the heat losses through the contact points are minimal, especially in transient conditions such as the ones encountered in this study. Two untreated sapphire windows (Edmund Optics) were placed in front of each face of the sample to ensure a containment of the fragments in case of loss of integrity of the sample. This sample-holder was then mounted on a 5-axis alignment stage (Newport, 9081-M) and placed at the center of the vacuum chamber. CAD views of the sample holder with an UO_2 disk are shown Figure 3.

Finally, a laser diode of a few tens of watts operating at 808 nm (LIMO, F200-DL808) was used on the non-heated face of the disk to pre-heat it to the desiderated temperature. Its beam is Gaussian with a waist ($1/e^2$) of 8.5 mm.

A schematic of the experimental setup is visible Figure 4.

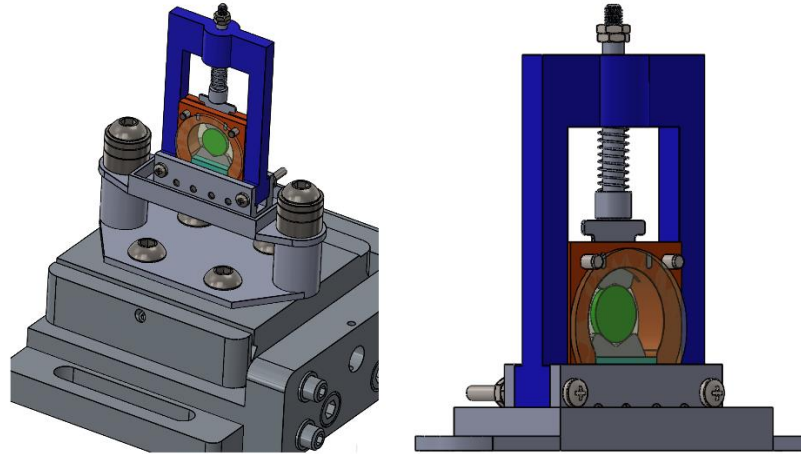


Figure 3: CAD view of the sample holder. The 5-axis alignment stage is visible on the left. All the parts directly in contact of the sample or around it are made of ZrO_2 , sapphire windows excepted.

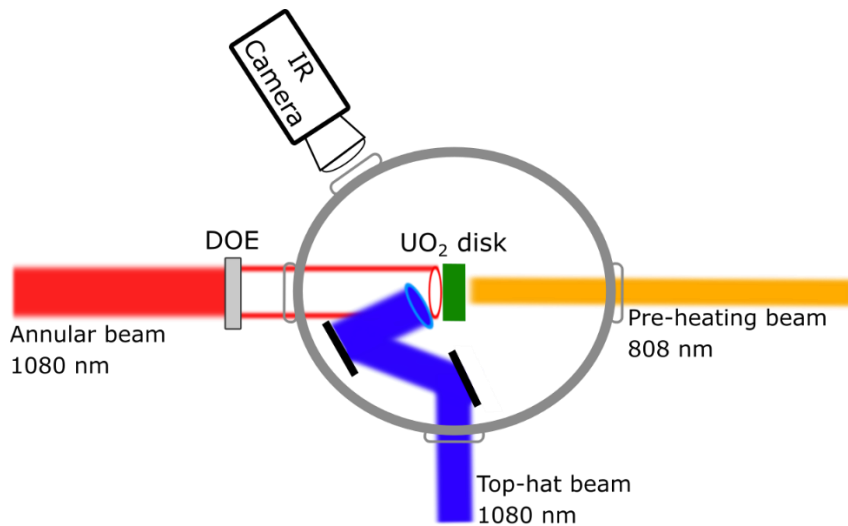


Figure 4: Schematic of the laser-heating experiment. The grey circle represents the vacuum chamber.

3) Temperature measurement:

The sample's surface temperature was measured with an high-performance infrared camera (FLIR, x6901sc-MWIR) operating within 3-5 μm wavelength range. The camera's rate of acquisition was set to 1000 Hz. The sample was observed by the camera at a 45° angle and synchronized with the laser pulses through a pulse generator (Berkeley Nucleonics, 577). In this study, the camera was equipped with a 100 mm focal length lens and a 0.75 inches (0.254 cm) extension ring was placed between the camera and the lens. The use of the extension ring improved the spatial resolution, reaching a value of 85 $\mu\text{m}/\text{pixel}$ for a field of view of 54x43 mm. The use of the extension ring did not induce any vignetting in the central region of the sensor used to observe the sample.

The optical impulse response (Point Spread Function – PSF) of this thermographic system (camera + lens + extension ring) was characterized with the knife-edge method [26–28]. This method is based on a measure of the Edge Spread Function (ESF) and enables the extrapolation of the PSF or the Modulation Transfert Function (MTF) of the imaging system. The ESF measurement was performed by positioning a sharp razor edge in front of a black-body source (Newport, Oriol) set to a temperature of 323.15 K (50 °C). The camera observed the edge through the same viewport used on the vacuum chamber and same distances as in experimental condition.

The estimated PSF of the camera is visible Figure 5 and can be approximated to a single Gaussian function with a waist ($1/e^2$) of 7 pixels ($\sim 600 \mu\text{m}$). It is important to note that the dimension of the PSF is thus larger than that of the annular beams, especially in the case of the focused one (0.1 mm waist). We can thus expect the thermographic measurements to be affected by the optical response of the camera. This should be taken into account during the analysis and interpretation of the measurements.

Finally, the emissivity of UO_2 is taken as 0.85 according to [29].

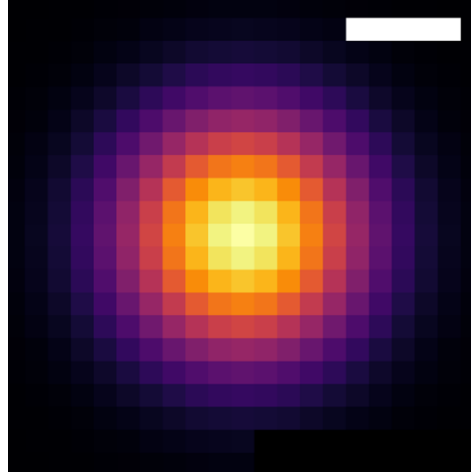


Figure 5: Estimated PSF with the knife-edge method. The scale bar has a width of 5 pixels.

III. Numerical tools:

The thermal simulations were performed on the thermal solver Cast3m of CEA [20] based on the finite elements method. The model considers a 2D axisymmetric representation of a cross-section of a disk. It considers radiative heat losses and laser loading is prescribed as a volumetric heat source. The non-linear heat flow equation is then solved to obtain the temperature distribution in the sample. The thermal properties are taken from [29,30].

A detailed description of this model and of the used properties for UO_2 is given in reference [17]. In this previous publication, the laser loading was described as a surface heat flux. We now can propose a refined analytical description of this laser loading as a volumetric heat source considering the optical characterization presented above.

1) Analytical description of the laser loading:

The absorption of the laser radiation in the depth of the sample is described with a Beer-Lambert law:

$$I(z) = I_0 e^{-\alpha_a z} \quad (1)$$

With I_0 the intensity distribution (W/m^2) at the surface of the sample. In 2D axi-symmetrical representation we thus have $I_0 = f(r)$. α_a is the coefficient of absorption in m^{-1} expressed as $\alpha_a = \frac{4\pi k}{\lambda}$, with k the coefficient of extinction and λ the wavelength. z is the depth relative to the surface.

The volumetric heat source is easily obtained by derivation:

$$Q(z) = -\frac{d}{dz}(I_0 \exp(-\alpha_a z)) = I_0 \alpha_a \exp(-\alpha_a z) \text{ (W/m}^3\text{)} \quad (2)$$

A. Annular beam:

The intensity distribution of the annular Gaussian beam I_0 (in W/m²) is given by the following expression:

$$I_0(r, R_{an}, \omega_{an}) = I_{max}(R_{an}, \omega_{an}, P_{an}) \exp\left(\frac{-2(r - R_{an})^2}{\omega_{an}^2}\right) \text{ (W/m}^2\text{)} \quad (3)$$

With I_{max} the peak intensity (in W/m²) of the Gaussian distribution at $r = R_{an}$, which is a function of R_{an} and ω_{an} , the radius and waist of the annular beam, and of beam's power P_{an} . Hence, we finally have:

$$Q_{an}(r, z) = I_{max} \exp\left(\frac{-2(r - R_{an})^2}{\omega_{an}^2}\right) \alpha_a \exp(-\alpha_a z) \text{ W/m}^3 \quad (4)$$

B. Top-Hat beam:

The intensity distribution of the Top-Hat beam is considered as homogeneous. To take into consideration the fact that the beam diameter is superior to the disk diameter, we consider the ratio the surface of the disk S_d and the surface of the beam S_b .

Hence, the heat source term is expressed as:

$$Q_{TH}(z) = \frac{P_{TH}}{S_b} \frac{S_d}{S_b} \times \alpha_a \exp(-\alpha_a z) \text{ W/m}^3 \quad (5)$$

With P_{TH} the power of the beam. Lasers' power have been measured with a calibrated calorimeter to ensure known values of P_{an} and of P_{TH} .

These source terms are then multiplied by a loss coefficient taking into account the total reflectance of the sample. The total reflectivity R_{tot} of the samples that combines specular and diffuse reflected light by the disks was measured with the same setup that the one used for the optical characterization of UO₂. This loss coefficient is around 15% at 1080 nm (laser's wavelength). Additionally, the reflection coefficient of the sapphire windows is also took into account. The losses occurring on the laser line were also measured (on mirrors, DOE, viewports etc.) and were found to be negligible (all optics have anti-reflection or high reflective coatings at 1080 nm).

2) Heat source term obtained from Monte-Carlo simulation

The previous expressions for the source terms assume a rectilinear propagation of the laser radiation through the sample without any scattering effects. However, the propagating laser radiation can potentially be scattered by grain boundaries or bulk porosities present in the material. The (bulk) scattering properties of a material is characterized by the angular distribution of the scattered light (i.e., its phase function) and the scattering coefficient α_s (m⁻¹). With the previously mentioned coefficient of absorption α_a (m⁻¹), we can thus express the total attenuation coefficient $\alpha_t = \alpha_a + \alpha_s$. To the best of our knowledge, there are no existing study in the literature regarding light scattering by polycrystalline UO₂. The determination of

these quantities is not trivial and would require, for example, an interpretation of spectrophotometric measurements through inverse Monte-Carlo simulation. As a first step, we hereinafter present a Monte-Carlo simulation model that was used to simulate the propagation of light in an UO_2 disk to obtain a heat source term that can then be used in the thermal simulation. This model was used to investigate the potential impact of the scattering phenomenon in the results section. It is important to note that if, in the present study, the material considered is close to its theoretical density (~95-98 %), nuclear ceramic can be subject to microstructural changes resulting in an increase in porosity of up to 20 %. As such it is also crucial to develop tools capable of accounting for these microstructural changes that would lead to a modification of the scattering power of the material.

The MCmatlab [31] program, a Monte Carlo simulation program coded in C++ and interfaced with MATLAB, was utilized for modeling light propagation in a 3D voxel space. The interested reader may refer to [32,33] for more information about Monte-Carlo simulations for light propagation in a scattering media.

In this study, we considered a cuboid of dimension $8.4 \times 8.4 \times (\text{DT} + 10^{-3}) \text{ mm}^3$ (DT being the Disk Thickness) divided into voxels of dimensions $5 \times 5 \times 1 \mu\text{m}^3$. Each voxel was assigned a value of α_a and α_s . The program considers the Henyey-Greenstein [34,35] phase function which reads:

$$P_{HG}(\theta, g) = \frac{1}{4\pi} \frac{1 - g^2}{(1 + g^2 - 2 \cdot g \cdot \cos\theta)^{3/2}}$$

(6)

With θ the angle of direction of propagation of the scattered light in radian and g the so-called anisotropy factor in the range $]-1;1[$. A negative value of g indicates a backward dominant scattering, 0 an isotropic scattering and a positive value a forward dominant scattering. Each voxel of the simulation space was thus also assigned a value of g .

Custom illumination profiles such as annular Gaussian beam can be generated by MCmatlab, making it the suitable tool for this study. It can also simulate refraction and Fresnel reflection at interfaces between media of different refractive index, provided that the interface is parallel to the xy -plane and we thus also assigned a refractive index value (n) for each voxel. The value for UO_2 was set to 2.1 based on the measurements and methodology presented in Section II.1) and in the supplementary file.

These values were assigned to each voxel in order to obtain the considered disk immersed in air with a thin layer ($10 \mu\text{m}$) of air on top of it. The disk was then illuminated with the annular or top-hat beam intensity distribution. A laser intensity volumetric distribution ($\text{W} \cdot \text{m}^{-2}$) within the disk was obtained at the end of the Monte-Carlo simulation. This intensity distribution was then multiplied by the absorption coefficient of UO_2 to obtain a volumetric heat source term ($\text{W} \cdot \text{m}^{-3}$) that was interpolated on the Cast3m's mesh. The resulting simulation sequence is illustrated in Figure 6.

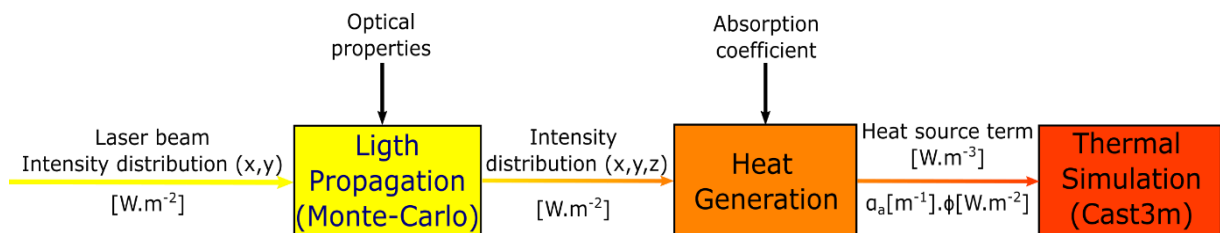


Figure 6: Schematic of the simulation sequence with the Monte-Carlo for light propagation simulation step

IV. Results and discussion:

1. Annular laser heating experiments:

Twelve annular laser heating experiments were performed on twelve different samples. All experiments had a pulse duration of 20 ms but different beam dimensions (focused or unfocused) and different initial temperature (circa 303 or 573 K, corresponding to 30 or 300 °C). The maximal measured temperature in this series is around 1523 K (1250 °C). The experimental parameters of this series are summarized in Table 1.

N°	Annular Beam Configuration	Power (W)	Initial Temperature (K)
AH 1	unfocused	120	308
AH 2	unfocused	120	583
AH 3	unfocused	320	613
AH 4	focused	120	573
AH 5	focused	250	573
AH 6	unfocused	120	328
AH 7	unfocused	146	333
AH 8	unfocused	120	593
AH 9	unfocused	320	593
AH 10	unfocused	456	593
AH 11	focused	120	348
AH 12	focused	120	603

Table 1: Test matrix for the Annular laser Heating (AH) experiments

A typical radial temperature profile measured on the vertical axis passing by the center of the disk with a false color image of the thermographic acquisition is visible on Figure 7. In this specific case, it is observed that the highest recorded temperature corresponds to the 19th acquired image. Given the acquisition rate of 1000 Hz and the synchronization of the camera and laser pulses, this observation is consistent with the expected temporal uncertainty of 1 ms.

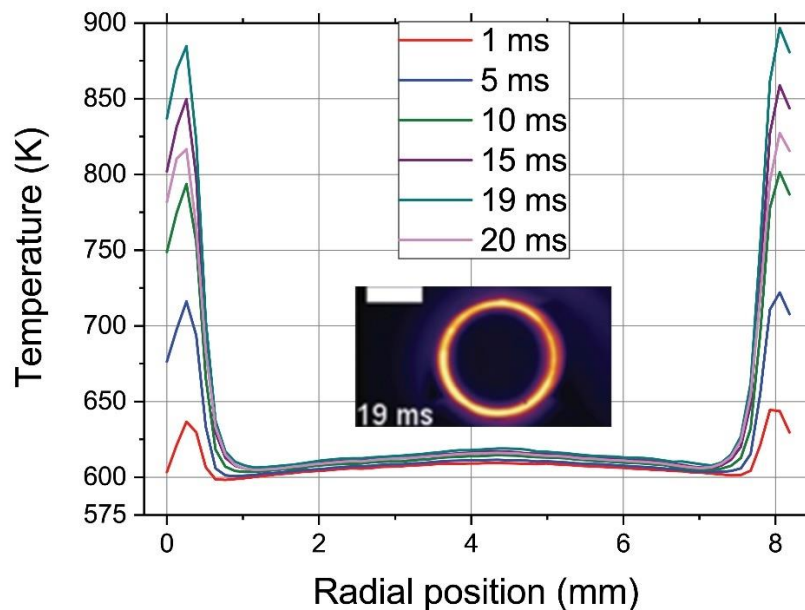


Figure 7: Radial temperature profiles measured for the AH11 heating sequence. Insert : false color image of the thermographic acquisition. Scale bar is 4 mm.

As stated in Section II. 2), it is anticipated that the optical response of the lens+camera system would greatly distort the thermal radiation image of the heated sample in regards of the annular beam dimensions versus the PSF dimensions. As expected, the calculated radial temperature profiles are consistently narrower, with the maximum measured temperature being up to twice as high as the measured value. Consequently, the measurement-calculation error in terms of peak temperature span from 40% to 120%.

To account for the blurring effect caused by camera aberrations, the simulated radial temperature profiles were convolved with the two-dimensional representation of the PSF, known as the Line Spread Function (LSF). This approach was chosen after unsuccessful attempts with available deconvolution algorithms. The convolution operation was implemented numerically using a Python script and the "convolve" function from the Scipy package. The LSF was previously normalized to have a numerical integral equal to 1.

Figure 8 presents the radial temperature profiles measured in two annular heating experiments (AH 11 and 2), along with the raw simulated and simulated-convolved radial temperature profiles. As the AH2 experiment initial temperature was around 573 K, the edge's temperature was also recorded during the transient. This effect is not seen for the AH11 experiment which had an initial temperature set around 303 K. The convolution operation significantly improves the agreement between the calculated and simulated temperature profiles. It is important to note that this implies that the simulated temperature profiles are arguably closer to the actual temperature profiles of the samples compared to the measured profiles, which are heavily distorted by camera aberrations.

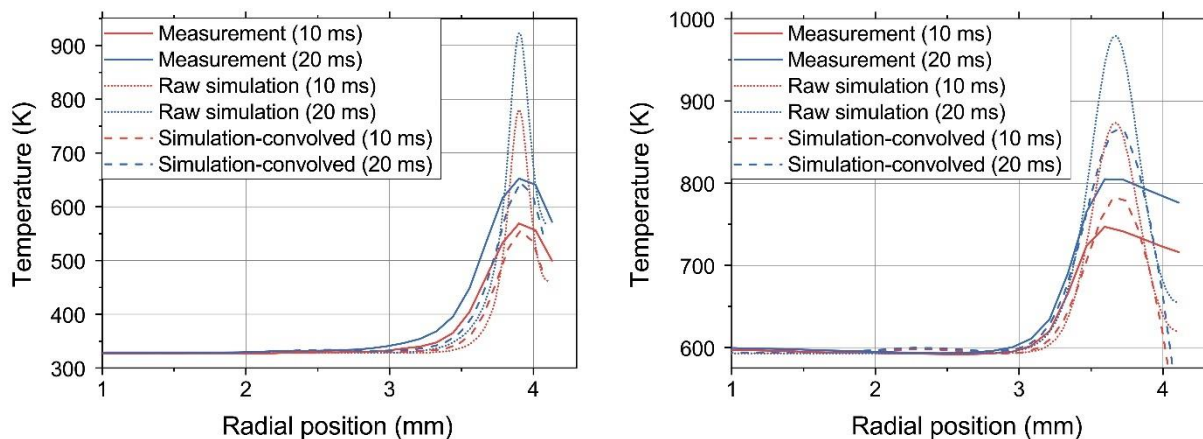


Figure 8: Measured, simulated and simulated-convolved radial temperatures profiles for the AH11 (left) and AH2 (right) experiments.

It is also interesting to examine the normalized temperature profiles. Figure 15 displays the normalized profiles at the end of the heating sequence for the same two annular heating experiments, AH 11 and AH 2. Upon observation, it is evident that the convolution performed with the LSF does not perfectly replicate the shape of the measured profiles. This suggests that scattering occurring within the sample's depth may not be negligible and could result in the broadening of the laser beam within the sample, subsequently affecting the corresponding heat source term.

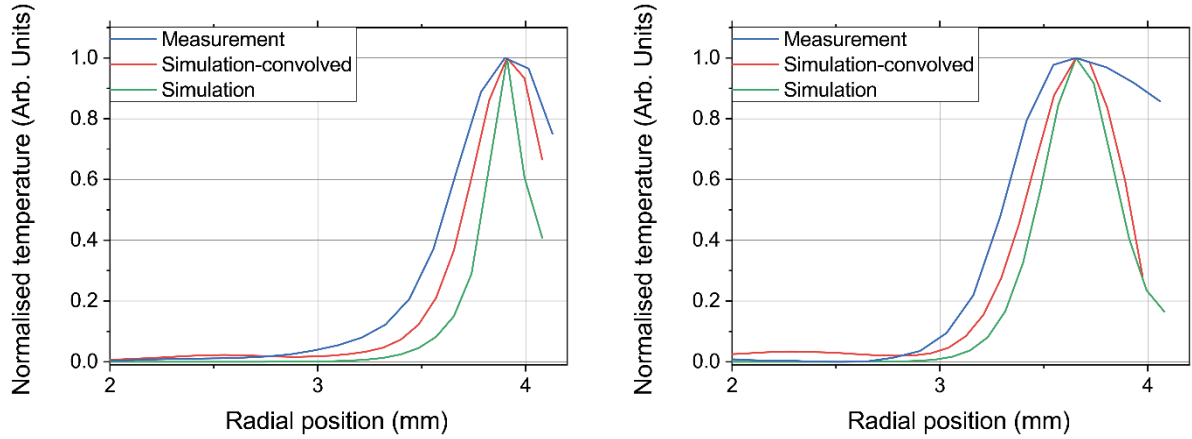


Figure 9: Measured, simulated and simulated-convolved normalised temperature profiles for the AH11 (left) and AH2 (right) heating experiments.

A. Phenomenological study of the impact of laser light scattering:

In this section, the Monte-Carlo solver presented in Section III was used to quantify the potential impact of scattering. To do so, a parametric sweep considering 27 sets of material parameters (α_a, α_s, g) was conducted. The values of the considered absorption and scattering coefficient are given Table 2. For each combination of this table, three source terms were calculated with g taking a value of 0.9, 0.75 or 0.5. The parameters were chosen in such a way that the coefficient of total attenuation (α_t) is equal to $7 \times 10^4 \text{ m}^{-1} \pm 5 \times 10^4$ with different proportion of scattering and absorption. This value of $7 \times 10^4 \text{ m}^{-1}$ roughly corresponds to the value of the coefficient of absorption determined previously where the scattering phenomena (i.e., $\alpha_t = \alpha_a$) was neglected.

$\delta_a (\mu\text{m})$	$\alpha_a (\text{m}^{-1})$	$\delta_a (\mu\text{m})$	$\alpha_s (\text{m}^{-1})$	$\alpha_t = \alpha_a + \alpha_s (\text{m}^{-1})$
20	5×10^4	10	1×10^5	1.5×10^5
10	1×10^5	20	5×10^5	1.5×10^5
25	4×10^4	50	2×10^4	6×10^4
25	4×10^4	75	1.33×10^4	5.33×10^4
50	2×10^4	50	2×10^4	4×10^4
50	2×10^4	25	4×10^4	6×10^4
75	1.33×10^4	75	1.33×10^4	2.67×10^4
75	1.33×10^4	25	4×10^4	5.33×10^4
100	1×10^4	100	1×10^4	2×10^4

Table 2: Values of absorbing and scattering coefficients taken for the parametric sweep in the Monte-Carlo simulations.

Figure 10 illustrates the temperature profiles and normalized temperature profiles obtained with the parametric sweep at the end of the AH12 experiment, along with a comparison to the analytical description of the heat-source term. In Figure 11, the axial temperature profiles at $r=R_{an}$ for the same experiment at the same time are displayed. The influence of the anisotropy coefficient g was found to be negligible, and therefore, the plotted profiles correspond to a g value of 0.75. Although the Monte-Carlo calculations demonstrates that scattering can indeed alter surface temperatures and the temperature distribution below the surface, we did not observe a significant broadening of the temperature profiles. This can be observed in the normalized profiles presented in Figure 10.

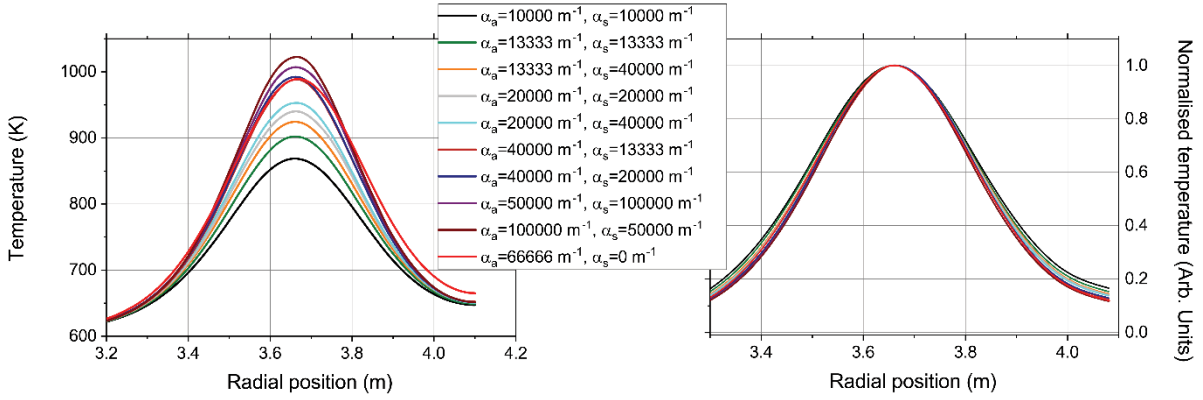


Figure 10: Temperature profiles (left) and normalized temperatures profiles (right) at the end of the AH2 experiment. Each curve corresponds to one set of parameters used in the Monte-Carlo simulation.

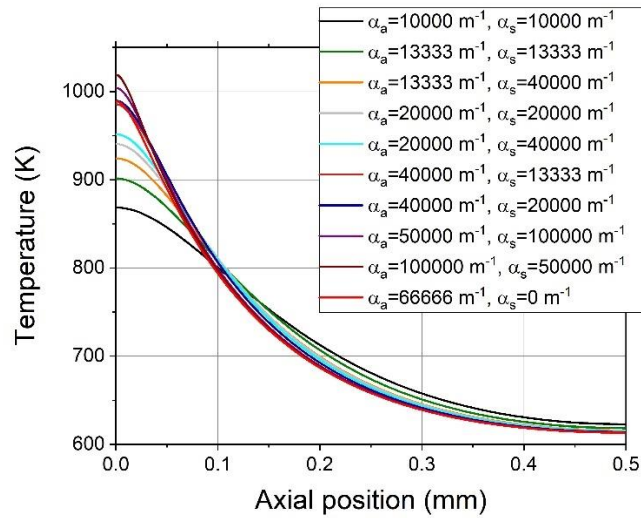


Figure 11: Temperature as a function of axial position at $r=R_{an}$ at the end of the AH2 experiment. Each curve corresponds to one set of parameters used in the Monte-Carlo simulation.

We can conclude that while the scattering effect can potentially play an important role, it does not appear to induce a significant broadening of the heat source term within the investigated parameters range. A complete characterization of the scattering behavior of the ceramic at the considered wavelength will however remain of interest if one wishes to simulate as accurately as possible the heat source term resulting from the laser loading.

From this parametric sweep, the set of parameters that led to the best overall improvement in the simulation-measurement comparison was retained. The best fit parameters are as follow:

- $\alpha_a = 2 \times 10^4 \text{ m}^{-1}$
- $\alpha_s = 2 \times 10^4 \text{ m}^{-1}$
- $g = 0.75$

Figure 12 presents a comparison of the peak surface temperature between the simulations and the measurements for the case of the analytical heat source term, analytical heat source term with the convolution by the LSF and Monte-Carlo heat source term with the convolution by the LSF, considering the aforementioned best fit parameters.

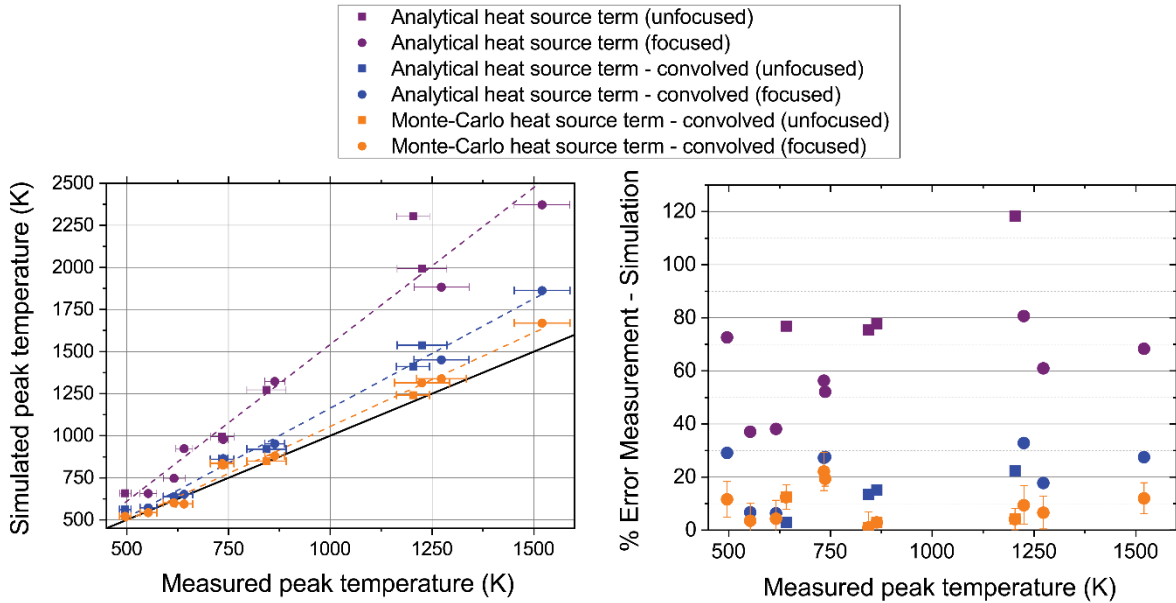


Figure 12: Annular heating experiments. Left: Measured peak temperatures versus simulated peak temperatures. Right: % Error measurements – simulations. The measurements were done at the end of the heating duration. Peak temperature was measured on 25 points on the circumference of the thermal ring. The error bar corresponds to the standard deviation of these 25 measures.

As one can see, taking both into accounts the camera’s PSF and the scattering phenomena leads to a fairly good result. We however stress again that the scattering parameters were not measured and are issued from a parametric sweep.

2. Homogeneous laser heating experiments:

Sixteen homogeneous laser heating experiments were performed on 16 different samples, involving variations in parameters such as duration (20 or 100 ms), power (ranging from 375 to 1900 W), and initial temperature (573 or 873 K, equivalent to 300 or 600 °C). The maximum temperatures recorded during these experiments span a range from around 773 to 2773 K, corresponding to 500 and 2500 °C.

N°	Duration (ms)	Power (W)	Initial temperature (K)
CH1	100	375	573
CH2	100	775	573
CH3	20	375	573
CH4	20	775	573
CH5	20	1160	573
CH6	20	1520	573
CH7	20	1900	573
CH8	100	375	873
CH9	100	775	873
CH10	100	1160	873
CH11	100	1520	873
CH12	20	375	873
CH13	20	775	873
CH14	20	1160	873
CH15	20	1520	873
CH16	20	1900	873

Table 3: Parameters of the homogenous heating experiments

Figure 13 displays typical temperature images obtained during the experiments, showcasing the case of the CH10 experiment. From the images, it can be observed that the heating is relatively homogeneous across the entire surface. The observed inhomogeneities can be attributed to the modulation of the laser beam, which is not perfectly uniform. Due to the relatively homogeneous temperature profiles, the impact of camera aberrations on the measurements is negligible.

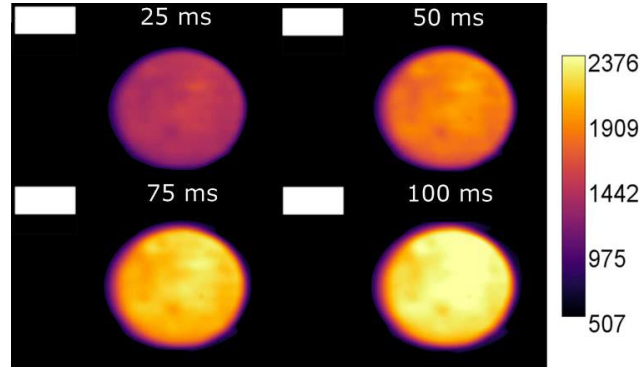


Figure 13: False color image for the CH10 heating experiment. Scale bar is 4 mm. Temperature scale is given in °C.

The comparison between the simulations using the analytical description of the laser loading and the measurements resulted in an error percentage of less than 15% for most experiments.

Additionally, the use of the Monte Carlo solver, considering the selected set of scattering parameters, did not lead to an improvement in the error percentage compared to the measurements. In fact, the simulated temperatures were consistently lower than the measured temperatures. The comparison between the measurements and simulations using both the analytical and statistical descriptions of the heat source term is summarized in Figure 20. These findings suggest that the parametric sweep conducted with the annular experiments, along with the selected set of parameters, may have compensated for certain error sources specific to the annular experiments. Therefore, a comprehensive analysis of other potential sources of uncertainty is now deemed necessary.

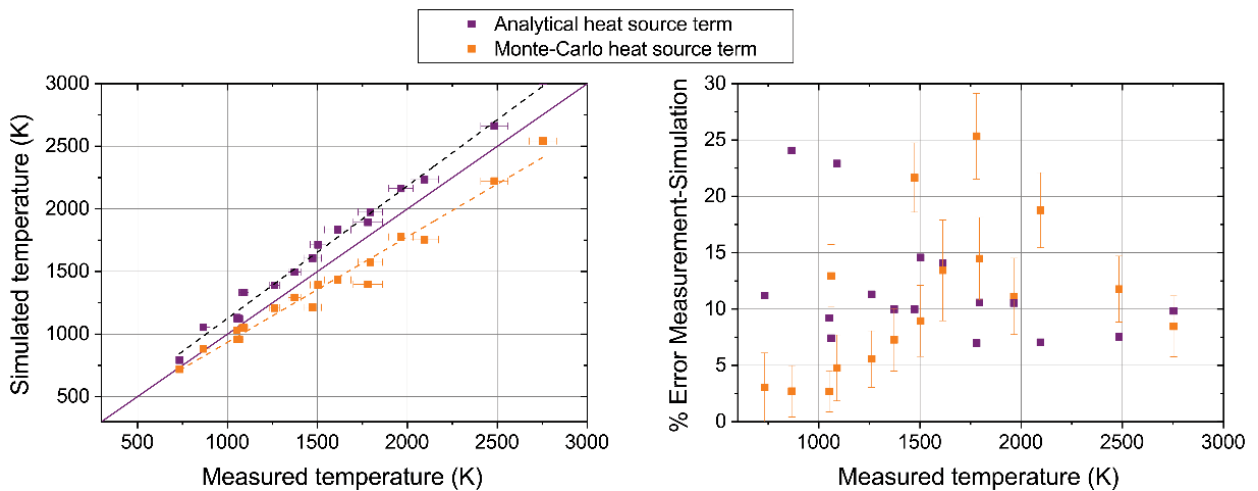


Figure 14 : Homogeneous heating experiments. Left: simulated temperature as a function of the measured temperature. Right: error percentage calculation-measurement. The measurements were done at the end of the heating duration. The error bar corresponds to the standard deviation of the measurement on the whole surface of the sample.

However, based on the observation that the error between the simulation and measurements does not vary significantly with increasing temperature during the annular or homogeneous heating experiments, it can be inferred that the emissivity and optical properties of the ceramic are not strongly dependent on temperature. This suggests that considering the evolution of emissivity and complex refractive index with temperature may not have a significant impact on reducing errors in the simulation or measurement.

Finally, in the case of a strongly localized heating such as the one obtained with the thinnest annular beam (waist at $1/e^2$ of $100\ \mu\text{m}$), it is possible that the thermally affected area was in any case insufficiently resolved with the lens at our disposal. The use of a better performing lens would enhance both the quality of the measurements and the precision of the ESF measurement, and ultimately reduce experimental errors.

3. Combined laser heating experiments:

In this section, we present two laser heating experiments that combine the annular laser beam and the Top-Hat laser beam. These experiments highlight the versatility of our approach in terms of spatial energy deposition and the resulting temperature profiles. The desired temperature profile, characterized by a uniform temperature increase across the entire sample surface with a peak at the periphery, closely resembles the temperature gradient experienced by nuclear fuel elements during a Reactivity Initiated Accident. In both cases the unfocused annular beam (waist at $1/e^2$ of $260\ \mu\text{m}$) was used. The experimental parameters for the two combined laser heating (CLH) experiments are summarized Table 4.

We report on Figure 15 the measured temperature profiles at different times for both experiments. These temperature profiles exhibit a nearly flat increase in temperature across the entire radius of the sample with a peak at its periphery, as anticipated. The maximum rate of temperature rise is approximately $75\ 000\ \text{K/s}$. The profiles display slight dissymmetry due to the characteristics of the Top-Hat beam, which slightly under or overheated one side of the sample. These experiments demonstrate the ability of our technique to induce complex temperature profiles on a sample by combining different beams of different intensity profiles.

N°	Duration (ms)	Annular beam power (W)	Homogeneous beam power (W)	Initial temperature (K)
CLH1	20	320	1540	873
CLH2	20	450	1450	873

Table 4: Experimental parameters of the combined laser heating experiments.

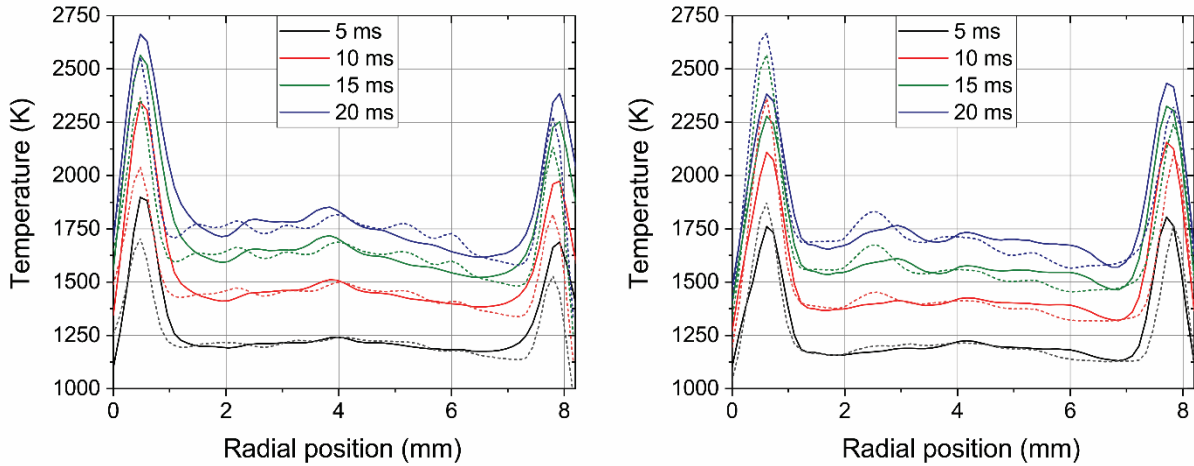


Figure 15: Measured temperature profiles for the CLH1 (left) and CLH2 (right) experiment. The lines correspond to the vertical axis passing through the center of the disk while the dotted lines correspond to the horizontal axis passing through the center of the disk.

V. Conclusions:

The aim of this study was to investigate the interaction between laser and UO₂ (depleted dense UO₂) in order to induce rapid transients and understand the resulting temperature gradient.

Initially, we conducted spectro-photometric measurements on low thickness ($< 55 \mu\text{m}$) samples of the same material. These measurements allowed us to determine the complex refractive index of polycrystalline UO₂. The refractive index values at 1080 nm were found to be approximately 2.1 (real part) and 0.006 (imaginary part).

Next, we presented our experimental approach, which built upon previous developments, along with the associated instruments and their characteristics. This included the impulse response of the thermographic camera used in the experiments. We also presented a 2D numerical model based on the finite element method to analyse the experimental results. Additionally, a 3D Monte-Carlo simulation scheme was introduced to simulate light propagation within the sample, taking into account scattering of the laser beam and its potential impact on the resulting temperature distribution.

For the highly localized annular heating experiments, we demonstrated that it is crucial to consider the impulse response of the camera in order to compare the simulation results with the measurements accurately. We then employed the Monte-Carlo simulation scheme to assess the potential influence of scattering within a specific range of optical parameters. By considering both the camera impulse response and light scattering, the error between the simulations and measurements was reduced from over 80% to less than 20%.

For the Top-Hat beam experiments, the thermographic acquisitions were found to be less affected by optical aberrations of the camera. A percentage error of approximately 15% was obtained without requiring the convolution step used in the annular case. This validates the analytical description of the laser loading, to some extent. However, it was observed that the previously obtained set of parameters for the Monte-Carlo simulation did not improve the comparison between measurements and simulations in this configuration. This indicates the necessity of a comprehensive experimental characterization of the scattering phenomenon. Additionally, determining the temperature dependence of the optical properties would ensure

more precise measurements and simulations, even though we anticipate that these properties are not highly temperature-dependent.

Furthermore, we presented two heating sequences where the annular and Top-Hat beams were combined to induce complex transients in the sample. The resulting temperature profiles qualitatively resemble the temperature profiles experienced by nuclear fuel elements during Reactivity Initiated Accident (RIA) transients in pressurized water reactors. In a previous publication [17], we demonstrated that the mechanical state in the sample during annular laser heating experiments also resemble, at the periphery of the sample, the state reached in a pellet during a RIA transient in a reactor. We now proposed in this study a complete characterization and interpretation of the thermal behaviour during these experiments and expanded the capabilities of our approach towards more complex thermal transient. This demonstrates the suitability of our technique for studying nuclear fuel under specific accidental conditions.

We believe that our approach can be extended to other applications for studying various materials at high temperatures or under prompt and specific thermal gradients, the induced thermal transient being heavily parametrizable.

Supplementary material:

The methodology employed for the determination of the complex refractive of dense polycrystalline UO_2 from spectrophotometric measurements is provided in the supplementary material provided with this study.

CRedit authorship contribution statement:

M. Reymond: Investigation, Methodology, Software, Writing – original draft. **T. Doualle:** Investigation. **J. Sercombe:** Conceptualization, Methodology, Validation. **M. Rocca:** Investigation, Software. **M. Nasselhsen:** Investigation, Software. **C. Colin:** Resources. **Y. Pontillon:** Conceptualization, Supervision, Validation, Writing – review & editing. **L. Gallais:** Conceptualization, Supervision, Validation, Writing – review & editing.

Acknowledgements:

The authors would like to thank Doris Druan from CEA Cadarache for the development and teaching of the technique used to realize the thin slides samples used for the determination of the complex refractive index of UO_2 .

M. Reymond and L. Gallais thank Anabela DaSilva from Institut Fresnel for its introduction to MCmatlab and help for the light scattering simulations.

Finally, we also thank EdF and Framatome for partial funding of this research and for the fruitful discussions.

Data available on request from the authors

The data that support the findings of this study are available from the corresponding author upon reasonable request.

References

- [1] R. Boehler, H.G. Musshoff, R. Ditz, G. Aquilanti, A. Trapananti, Portable laser-heating stand for synchrotron applications, *Rev. Sci. Instrum.* 80 (2009) 045103. <https://doi.org/10.1063/1.3115183>.
- [2] S. Anzellini, S. Boccato, A Practical Review of the Laser-Heated Diamond Anvil Cell for University Laboratories and Synchrotron Applications, (2020) 28.

- [3] M. Minissale, C. Pardanaud, R. Bisson, L. Gallais, The temperature dependence of optical properties of tungsten in the visible and near-infrared domains: an experimental and theoretical study, *J. Phys. Appl. Phys.* 50 (2017) 455601. <https://doi.org/10.1088/1361-6463/aa81f3>.
- [4] L. Gallais, T. Vidal, E. Lescoute, Y. Pontillon, J.L. Rullier, High power continuous wave laser heating of graphite in a high temperature range up to 3800 K, *J. Appl. Phys.* 129 (2021) 043102. <https://doi.org/10.1063/5.0033530>.
- [5] D. Manara, C. Ronchi, M. Sheindlin, Solidus and liquidus of UO_2+x from high-pressure melting experiments, *High Temp.-High Press.* 35/36 (2003) 25–33. <https://doi.org/10.1068/htjr088>.
- [6] D. Manara, R. Pflieger, M. Sheindlin, Advances in the Experimental Determination of the Uranium–Oxygen Phase Diagram at High Temperature, *Int. J. Thermophys.* 26 (2005) 1193–1206. <https://doi.org/10.1007/s10765-005-6711-y>.
- [7] F. De Bruycker, K. Boboridis, P. Pöml, R. Eloirdi, R.J.M. Konings, D. Manara, The melting behaviour of plutonium dioxide: A laser-heating study, *J. Nucl. Mater.* 416 (2011) 166–172. <https://doi.org/10.1016/j.jnucmat.2010.11.030>.
- [8] D. Prieur, F. Lebreton, M. Caisso, P.M. Martin, A.C. Scheinost, T. Delahaye, D. Manara, Melting behaviour of americium-doped uranium dioxide, *J. Chem. Thermodyn.* 97 (2016) 244–252. <https://doi.org/10.1016/j.jct.2016.02.003>.
- [9] L. Vlahovic, D. Staicu, A. Küst, R.J.M. Konings, Thermal diffusivity of UO_2 up to the melting point, *J. Nucl. Mater.* 499 (2018) 504–511. <https://doi.org/10.1016/j.jnucmat.2017.11.050>.
- [10] T.R. Pavlov, M.R. Wenman, L. Vlahovic, D. Robba, R.J.M. Konings, P. Van Uffelen, R.W. Grimes, Measurement and interpretation of the thermo-physical properties of UO_2 at high temperatures: The viral effect of oxygen defects, *Acta Mater.* 139 (2017) 138–154. <https://doi.org/10.1016/j.actamat.2017.07.060>.
- [11] T.R. Pavlov, D. Staicu, L. Vlahovic, R.J.M. Konings, P. Van Uffelen, M.R. Wenman, A new method for the characterization of temperature dependent thermo-physical properties, *Int. J. Therm. Sci.* 124 (2018) 98–109. <https://doi.org/10.1016/j.ijthermalsci.2017.10.008>.
- [12] M. Bober, J. Singer, K. Wagner, Spectral Reflectivity and Emissivity Measurements of Solid and Liquid UO_2 at 458, 514.5 and 647 nm as a Function of Polarization and Angle of Incidence, Kernforschungszentrum Karlsruhe - Institut für Neutronenphysik und Reaktortechnik, 1980.
- [13] M. Bober, J. Singer, Determination of the Optical Constants of Liquid UO_2 in the Near Infrared at 1064 nm, *Nucl. Sci. Eng.* 105 (1990) 341–348. <https://doi.org/10.13182/NSE90-A21469>.
- [14] M. Joseph, N. Sivakumar, P. Manoravi, Laser-Induced Vaporization–Mass Spectrometry Studies on Refractory Materials at Ultrahigh Temperatures, in: *Mater. Extreme Cond.*, Elsevier, 2017: pp. 533–573. <https://doi.org/10.1016/B978-0-12-801300-7.00015-2>.
- [15] R. Pflieger, M. Sheindlin, J.-Y. Colle, Thermodynamics of Refractory Nuclear Materials Studied by Mass Spectrometry of Laser-Produced Vapors, *Int. J. Thermophys.* 26 (2005) 1075–1093. <https://doi.org/10.1007/s10765-005-6686-8>.
- [16] T. Vidal, L. Gallais, J. Faucheux, H. Capdevila, J. Sercombe, Y. Pontillon, Simulation of reactivity initiated accident thermal transients on nuclear fuels with laser remote heating, *J. Nucl. Mater.* 530 (2020) 151944. <https://doi.org/10.1016/j.jnucmat.2019.151944>.
- [17] M. Reymond, J. Sercombe, L. Gallais, T. Doualle, Y. Pontillon, Thermo-mechanical simulations of laser heating experiments on UO_2 , *J. Nucl. Mater.* 557 (2021) 153220. <https://doi.org/10.1016/j.jnucmat.2021.153220>.
- [18] T. Doualle, V. Le Guillous, V. Klosek, C. Onofri-Marroncle, M. Reymond, L. Gallais, Y. Pontillon, Development of UO_2 thermal diffusivity measurement with laser techniques, *EPJ Web Conf.* 253 (2021) 07005. <https://doi.org/10.1051/epjconf/202125307005>.

- [19] I. Guénot-Delahaie, J. Sercombe, T. Helfer, P. Goldbronn, É. Fédérici, T. Le Jolu, A. Parrot, C. Delafoy, C. Bernaudat, Simulation of reactivity-initiated accident transients on UO₂-M5® fuel rods with ALCYONE V1.4 fuel performance code, *Nucl. Eng. Technol.* 50 (2018) 268–279. <https://doi.org/10.1016/j.net.2017.12.006>.
- [20] Cast3M, (2019). <http://www-cast3m.cea.fr/>.
- [21] P. Ruello, K.D. Becker, K. Ullrich, L. Desgranges, C. Petot, G. Petot-Ervas, Thermal variation of the optical absorption of UO₂: determination of the small polaron self-energy, *J. Nucl. Mater.* 328 (2004) 46–54. <https://doi.org/10.1016/j.jnucmat.2004.03.002>.
- [22] R.J. Ackermann, R.J. Thorn, G.H. Winslow, Visible and Ultraviolet Absorption Properties of Uranium Dioxide Films, *J Opt Soc Am.* 49 (1959) 1107–1111. <https://doi.org/10.1364/JOSA.49.001107>.
- [23] T.T. Meek, B. von Roedern, P.G. Clem, R.J. Hanrahan, Some optical properties of intrinsic and doped UO₂ thin films, *Mater. Lett.* 59 (2005) 1085–1088. <https://doi.org/10.1016/j.matlet.2004.12.012>.
- [24] T.R. Griffiths, H.V. St. A. Hubbard, Absorption spectrum of single-crystal UO₂: Identification of and effect of temperature on the peak positions of essentially all optical transitions in the visible to near infrared regions using derivative spectroscopy, *J. Nucl. Mater.* 185 (1991) 243–259. [https://doi.org/10.1016/0022-3115\(91\)90510-E](https://doi.org/10.1016/0022-3115(91)90510-E).
- [25] M. Minissale, A. Durif, P. Hiret, T. Vidal, J. Faucheux, M. Lenci, M. Mondon, G. Kermouche, Y. Pontillon, C. Grisolia, M. Richou, L. Gallais, A high power laser facility to conduct annealing tests at high temperature, *Rev. Sci. Instrum.* 91 (2020) 035102. <https://doi.org/10.1063/1.5133741>.
- [26] M. Etribeau, P. Magnan, Fast MTF measurement of CMOS imagers using ISO 12333 slanted-edge methodology, in: J.-P. Chatard, P.N.J. Dennis (Eds.), *St. Etienne, France, 2004*: p. 243. <https://doi.org/10.1117/12.513320>.
- [27] B.M. Lane, E.P. Whinton, *Calibration and Measurement Procedures for a High Magnification Thermal Camera*, National Institute of Standards and Technology, 2016. <https://doi.org/10.6028/NIST.IR.8098>.
- [28] J.M. Mooney, Measurement of the modulation transfer function of infrared cameras, *Opt. Eng.* 34 (1995) 1808. <https://doi.org/10.1117/12.203133>.
- [29] International Atomic Energy Agency, *Thermophysical properties database of materials for light water reactors and heavy water reactors: final report of a coordinated research project, 1999-2005.*, International Atomic Energy Agency, Vienna, 2006.
- [30] J.K. Fink, Thermophysical properties of uranium dioxide, *J. Nucl. Mater.* 279 (1999) 1–18. [https://doi.org/10.1016/S0022-3115\(99\)00273-1](https://doi.org/10.1016/S0022-3115(99)00273-1).
- [31] D. Marti, R.N. Aasbjerg, P.E. Andersen, A.K. Hansen, MCmatlab: an open-source, user-friendly, MATLAB-integrated three-dimensional Monte Carlo light transport solver with heat diffusion and tissue damage, *J. Biomed. Opt.* 23 (2018) 1. <https://doi.org/10.1117/1.JBO.23.12.121622>.
- [32] B.C. Wilson, G. Adam, A Monte Carlo model for the absorption and flux distributions of light in tissue: Absorption and flux of light in tissue, *Med. Phys.* 10 (1983) 824–830. <https://doi.org/10.1118/1.595361>.
- [33] L. Wang, MCML - Monte Carlo modeling of light transport in multi-layered tissues, *Comput. Methods Programs Biomed.* (1995) 16.
- [34] L.G. Henyey, J.L. Greenstein, Diffuse radiation in the galaxy, *Astrophys. J.* 93 (1941) 70–83.
- [35] T. Binzoni, T.S. Leung, A.H. Gandjbakhche, D. Rüfenacht, D.T. Delpy, The use of the Henyey–Greenstein phase function in Monte Carlo simulations in biomedical optics, *Phys. Med. Biol.* 51 (2006) N313–N322. <https://doi.org/10.1088/0031-9155/51/17/N04>.